



Array configuration studies for the Square Kilometre Array – Implementation of figures of merit based on spatial dynamic range

Dharam Vir Lal *

Max-Planck-Institut für Radioastronomie, Auf dem Hügel 69, 53121 Bonn, Germany

E-mail: dharam@mpifr-bonn.mpg.de

Andrei P. Lobanov

Max-Planck-Institut für Radioastronomie, Auf dem Hügel 69, 53121 Bonn, Germany

E-mail: alobanov@mpifr-bonn.mpg.de

Sergio Jiménez-Monferrer

Max-Planck-Institut für Radioastronomie, Auf dem Hügel 69, 53121 Bonn, Germany

and

Universidad de Valencia, Dr. Moliner 50, 46100 Burjassot, Valencia, Spain

E-mail: sergio.jimenez@uv.es

The Square Kilometre Array (SKA) will be operating at the time when several new large optical, X-ray and Gamma-ray facilities are expected to be working. To make SKA both competitive and complementary to these large facilities, thorough design studies are needed, focused in particular on imaging performance of the array. One of the crucial aspects of such studies is the choice of the array configuration, which affects substantially the resolution, rms noise, sidelobe level and dynamic range achievable with the SKA. We present here a quantitative assessment of the effect of the array configuration on imaging performance of the SKA, introducing the spatial dynamic range (SDR) and a measure of incompleteness of the Fourier domain coverage ($\Delta u/u$) as prime figures of merit.

*This work has been supported by the European Community Framework Programme 6, Square Kilometer Array Design Studies (SKADS), contract no 011938.

1. Introduction

The demanding breadth of the science case and technical specifications of the Square Kilometre Array (SKA) makes the design of the array a complex, multi-dimensional undertaking (Jones 2003). Although a number of factors may limit the performance of the SKA, including radio frequency interference, atmospheric and ionospheric effects (Perley 1999, Thompson et al. 1986), the array configuration is one of the most critical aspects of the instrument design (ISPO 2006), as it will be very difficult to modify or modernise the station locations after the construction phase has finished.

Several approaches have been exercised in order to obtain an optimised array configuration (Conway 1998, Bregman 2000, Conway 2000a, 2000b, Kogan 2000a, 2000b, Noordam 2001, Cohan et al. 2004, Bregman 2005, Kogan & Cohen 2005, Lonsdale 2005, Morita & Holdaway 2005). Judgement of quality and fidelity of synthesised images is typically made by estimating the "dynamic range", the ratio between the peak brightness on the image and the r.m.s. noise in a region free of emission of the image (Perley 1999). High dynamic range is necessary for imaging a high-contrast feature, which is a key requirement for the SKA. SKA design goal for the synthesised image dynamic range is 10^6 at 1.4 GHz (Wright 2002, 2004).

Alongside the dynamic range, one of the basic figures of merit (FoM) characterising imaging performance of an interferometer is the spatial dynamic range (SDR) quantifying the range of spatial scales that can be reconstructed from interferometer data (Lobanov 2003). The SDR of an interferometer depends on a number of instrument parameters, including the integration time of the correlator, channel bandwidth, and the coverage of the Fourier domain (uv -coverage). The latter factor poses most stringent constraints on the design, particularly for arrays with a relatively small number of elements. The quality of the uv -coverage can be expressed by the uv -gap parameter or $\Delta u/u$, characterising the relative size of "holes" in the Fourier plane. Basic analytical estimates indicate that the SKA should have $\Delta u/u \lesssim 0.2$ (Lobanov 2003) over the entire range of baselines to provide sufficient imaging capabilities and warrant that the SDR of the SKA would not be uv -coverage limited.

The SKA configuration must provide uv -coverages that satisfy several key requirements derived from the prime science goals of the instrument: (i) good snapshot and deep imaging over 1 degree field of view, (ii) high brightness temperature (T_b) for extended objects, (iii) dense core for transients/pulsar/SETI, and (iv) long baselines for milli-arcsecond imaging. The combination of these requirements with the benchmark figures for the dynamic range of continuum (10^6) and spectral line (10^5) observations poses a substantial challenge for the array design and for the antenna distribution in particular.

A commonly used approach to designing the antenna configuration for an interferometric array relies on optimising the uv -coverage by minimising sidelobes or providing a desired beam shape (cf., Cornwell 1986, Kogan 2000a, 2000b). This approach assumes implicitly that the field of view is not crowded and the target objects are marginally resolved (so that the structural information can be recovered efficiently even if a substantial fraction of spatial frequencies is undersampled). Neither of these two assumptions will be correct for the SKA operating in the μJy regime. This complication requires additional constraints and considerations to be employed in order to warrant successful imaging of all spatial scales sampled by the interferometer.

This issue can be addressed effectively by ensuring a constant $\Delta u/u$ over the entire range of baselines, which will provide equal sensitivity to all spatial scales sampled by an interferometer and realize the full spatial dynamic range of the instrument.

2. Spatial dynamic range of an interferometer

Spatial dynamic range of an interferometer is determined by several major factors related to details of signal processing, design of the primary receiving element, and distribution of the collecting area of an array (Lobanov 2003). The maximum achievable spatial dynamic range (SDR_{FoV}), is given by the ratio of the field of view and the synthesised beam (HPBW). For an array composed of parabolic antennas

$$\text{SDR}_{\text{FoV}} \approx 0.80 \frac{B_{\text{max}}}{\eta_a^{0.5} D},$$

where, B_{max} is the longest baseline in the array, η_a is the aperture efficiency, and D is the diameter of the antenna. However, SDR_{FoV} can be typically achieved only at the shortest baselines. The SDR is significantly reduced at the highest instrumental resolution, due to finite bandwidth and integration time, and incomplete sampling of the Fourier domain. Applying an averaging time of τ_a to interferometric data limits the maximum size θ_a , of structure detected at full sensitivity to $\theta_a = c (v_{\text{obs}} \omega_e \tau_a B_{\text{max}})^{-1}$ (Bridle & Schwab 1999), where v_{obs} is the observing frequency and ω_e is the angular rotation speed of the Earth. Relating this size to the HPBW of the interferometer yields the maximum SDR that can be achieved at a given integration time:

$$\text{SDR}_{\tau} \approx (\omega_e \tau_a)^{-1} \approx 1.13 \times 10^4 \tau^{-1}.$$

Bandwidth smearing due to a finite fractional bandwidth, Δv , leads to a reduction in the peak response $R_{\Delta v} = (1 + \Delta v \theta_v / \theta_{\text{HPBW}})^{-1/2}$ (assuming a Gaussian bandpass and circular Gaussian tapering; see Bridle & Schwab 1999). The resulting limit on spatial dynamic range, $\text{SDR}_{\Delta v}$, can be approximated by the ratio $\theta_v / \theta_{\text{HPBW}}$, which gives

$$\text{SDR}_{\Delta v} \approx \Delta v^{-1} (R_{\Delta v}^{-2} - 1)^{1/2},$$

with $R_{\Delta v} \leq 0.75$ typically assumed. Finally, incomplete sampling of the Fourier space yields $\text{SDR}_{\Delta u} < \text{SDR}_{\text{FOV}}$. The magnitude of the SDR reduction can be expressed in terms of the "uv-gap" parameter, $\Delta u/u$, that can be defined as follows: $\Delta u/u = (u_2 - u_1)/u_1$, where u_1, u_2 ($u_2 > u_1$) are the uv -radii of two adjacent baselines (sampling respective structural scales $\theta_{1,2} = 1/u_{1,2}$, with $\theta_1 > \theta_2$). Applying the assumptions used for deriving $\text{SDR}_{\Delta v}$ gives a synthesised beam that can be well-approximated by a two-dimensional Gaussian. Then, for structures partially resolved at u_2 , the smallest resolvable size (or variation of the size) can be estimated by requiring that a difference in visibility amplitudes $V(u_1)$ and $V(u_2)$ can be detected at a given SNR. This approach is similar to the one applied to determining resolution limits of an interferometer (*c.f.*, Lobanov et al. 2001, Lobanov 2005), and for $\text{SNR} \gg 1$ it yields $\theta_2/\theta_1 = (\pi/4)[\ln 2 \ln(\text{SNR})]^{-1/2}$. The ratio θ_2/θ_1 can be represented by the term $1 + \Delta u/u$. With this term, the expression $\text{SNR}_{\Delta u} = \exp[\pi^2(1 + \Delta u/u)^2 / (16 \ln 2)]$ gives the relation between $\Delta u/u$ and the SNR required for detecting emission on spatial scales corresponding to the (u_1, u_2) range. In case of a filled aperture, for which

$\Delta u/u \rightarrow 0$, the corresponding $\text{SNR}_{\Delta u} = \text{SNR}_{\Delta u/u=0} = \exp[\pi^2/(16 \ln 2)]$ and $\text{SDR}_{\Delta u} = \text{SDR}_{\text{FOV}}$. For partially filled apertures, the ratio $\text{SDR}_{\Delta u}/\text{SDR}_{\text{FOV}}$ can be estimated from the ratio $\text{SNR}_0/\text{SNR}_{\Delta u}$, which then gives

$$\text{SDR}_{\Delta u} = \text{SDR}_{\text{FOV}} / \exp \left[\frac{\pi^2}{16 \ln 2} \frac{\Delta u}{u} \left(\frac{\Delta u}{u} + 2 \right) \right].$$

Strictly speaking, the uv -gap parameter is a function of the location (u, θ) in the uv -plane (with θ describing the position angle), and it should be represented by a density field in the uv -plane. We will apply this description for making assessments of realistic uv -coverages obtained from our simulations.

The $1/\exp$ factor in the expression for SDR_{uv} , calculated for two uv -points u_1 and u_2 , essentially provides an estimate of a fraction of power that can be recovered between the respective angular scales (θ_2, θ_1) from the sky brightness distribution. When an average value of $\Delta u/u$ over the entire uv -coverage is determined, the $1/\exp$ factor can be taken as a measure of ratio between the largest detectable structure and the primary beam (FOV) of individual array elements (under condition that the largest detectable size obtained from $\Delta u/u$ is smaller than the largest angular scale given by $1/u_{\min}$).

For an idealised, circular uv -coverage obtained with a regular array (*i.e.* logarithmic-spiral) with N stations organised in M arms extending over a range of baselines (B_{\min}, B_{\max}) , the uv -gap can be approximated by $\Delta u/u \approx (B_{\max}/B_{\min})^\xi - 1$, with $\xi = M/N$ for baselines between antennas on a single arm, and $\xi = 1/N$ for all baselines. For instruments with multi-frequency synthesis (MFS) implemented, $\Delta u/u$ should be substituted by $\Delta u/u - \Delta v_{\text{mfs}}$, where, Δv_{mfs} is the fractional bandwidth over which the multi-frequency synthesis is being performed. It should be noted that MFS will be not as effective improving $\Delta u/u$ for sources near the equator.

In real observations, the actual SDR is determined by the most conservative of the estimates provided above. The simulations presented below will focus on $\text{SDR}_{\Delta u}$, assuming implicitly that the instrument is designed so that $\text{SDR}_{\Delta u} \geq \text{SDR}_{\Delta v}$ and $\text{SDR}_{\Delta u} \geq \text{SDR}_\tau$. Under this assumption, we investigate the relation between different array configurations as described by $\Delta u/u$ and resulting image properties described by the rms noise, dynamic range, and structural sensitivity of the array.

3. Relation between uv -coverage and imaging capabilities of an interferometer

In order to provide a quantitative measure of the effect of array configuration on imaging performance of an interferometer, we simulate a set of an idealised array configurations, each providing

$$\frac{\Delta u}{u} \equiv \text{const}$$

over the entire range of u and θ . It should be noted that these configurations are introduced solely for the purpose of analysing the dependence of SDR on the uv -coverage, and they are not intended to serve as prototype configurations for the SKA

We generate the test array configurations by considering an equiangular, planar logarithmic spiral and projecting this spiral on Earth's surface and determine the locations of individual stations (*i.e.*, latitudes and longitudes) using World GEOD system 1984 (Heiskanen & Moritz 1967). We apply Halley's third-order formula (Fukushima 2006), a modification of Borkowski's method

Table 1: Telescope settings for the generation of a range of visibility datasets.

Parameter	Value
Frequency	L band (1.4 GHz)
Antenna	SEFD= 335 K [†]
Bandwidth	3.2 MHz
No. of channels	1
Direction (J2000)	00:00:00 +90.00.00
Elevation limit	12 deg
Shadow limit	0.001 [‡]
Start_time (IAT)	22/08/2007 / 06:00
Stop_time (IAT)	22/08/2007 / 18:00

Note: [†] – similar to the system independent flux density (SEFD) of a VLA antenna; [‡] – shadow limit is set such as not to constrain the uv -coverages obtained.

Table 2: Input group of source components used for the generation of simulated visibility datasets.

Source size	RA (J2000)	Dec (J2000)	Flux density (Jy)
0.1' × 0.1'	03:00:00	88.00.00	8.0
1.0' × 1.0'	08:00:00	88.30.00	4.0
1.2' × 0.4'	16:00:00	89.00.00	1.2
3.0' × 1.0'	21:00:00	88.00.00	3.0
12.0' × 4.0'	06:00:00	88.00.00	12.0
42.0' × 14.0'	18:00:00	88.00.00	42.0
120.0' × 40.0'	00:00:00	90.00.00	120.0

(Borkowski 1989), to transform Cartesian to geodetic coordinates. This method is sufficiently precise; the maximum error of the latitude and the relative height is less than $6 \mu\text{arcsec}$ for the range of height, $-10 \text{ km} \leq \text{height} \leq 30,000 \text{ km}$, and is stable in the sense that it converges for all coordinates including the near-geocentre region and near-polar axis region. We then transform these coordinates to obtain ECEF (Earth Centered Earth Fixed) coordinates using a glish script, and produce an input array configuration file. The actual dimensions of the simulated array are chosen such that baseline non-coplanarity is negligible and no w -term correction is required. This does not affect conclusions obtained from the simulations, which are generic and can be applied to evaluate imaging performance of any interferometric array of arbitrary configuration and extent.

In order to generate uv -coverages satisfying the condition

$$\frac{\Delta u}{u}(u, \phi) \equiv \text{const},$$

we place the array center at the North Pole, and consider a fiducial field centered at a 90 deg declination (which yields circular uv -coverages that can be described by a single value of $\Delta u/u$). The corre-

sponding visibility datasets have been generated in `aips++` (ver 1.9, build 1556; `casa.nrao.edu`). Imaging has been done with AIPS package (`www.aips.nrao.edu`). Several Fortran programs and glish scripts have been developed and used to automate the process and provide a structured, uniform, repeatable and robust processing.

We generate datasets for full track observations (IAT 6:00–18:00 hrs), using a range of integration times at a frequency of 1.4 GHz and with a 3.2 MHz bandwidth (see Table 1). Antenna sensitivity (listed in Table 1) are assumed to be similar to a dish of Very Large Array (VLA). The simulator does not take into account the effect of the primary beam on imaging. An elevation limit (horizon mask) of 12 deg and a shadow limit (maximum fraction of geometrically shadowed area before flagging occurs) of 0.1 per cent was introduced.

We produce a number of array configurations corresponding to different values of $\Delta u/u$ and use them to obtain visibility datasets for the chosen model brightness distribution (see Table 2). We repeat this exercise for all generated array configurations and perform identical pipeline analysis, to ensure a self-consistent comparison of basic characteristics of the resulting dirty and CLEAN-ed images.

3.1 Simulations

This section describes simulations and analysis of array configurations providing equal uv -gap at all baseline lengths.

We have tried two different algorithms for generating array configurations with a given $\Delta u/u = \text{const}$ for all baselines. Both algorithms have employed a logarithmic spiral geometry, but differed in the realisation of changing the characteristic value of $\Delta u/u$ from one configuration to another. In the first algorithm, the total number of stations was kept constant, while the baseline spread was gradually increased. In the second approach, the baseline spread was kept constant, and changing $\Delta u/u$ was achieved by changing the total number of antennas in the array. We have found that the second approach is superior for maintaining a constant noise level for different array configurations, and we adopted it as the basis for our simulations. In this set of simulations, the largest baseline length, $B_{\text{max}} = 5$ km is kept constant and different values of $\Delta u/u$ are realized by varying the total number of antennas N located on a single arm of an equiangular, logarithmic spiral. Fig. 1 gives an example of an simulated snapshot uv -coverage generated using this approach.

We consider only baselines to the station at the origin of the array and generate a range of visibility datasets to probe the uv -gap parameter from 0.19 ($N = 50$) to 0.01 ($N = 640$). The simulated integration time is set to 1 second, and the resulting sampling times range from 12.5 seconds (one uv -point every 12.5 seconds) for $N = 50$ to 160 seconds for $N = 640$. With these settings, we produce visibility datasets for full track uv -coverages for each of the array configuration.

>From the simulated data, we produce both dirty and CLEAN images, of $8192 \text{ pixels} \times 8192 \text{ pixels}$ in size, with a pixel size of 3 arcsec. The dirty images obtained for several different simulated configurations are shown in Fig. 2. The respective interferometer beam cuts are shown in Fig. 3. The CLEAN images were obtained using AIPS task IMAGR applied to 499 facets spread across a ~ 50 square degree field. It should be noted that the CLEAN algorithm has been applied non-interactively (*i.e.*, with the same set of CLEAN parameters for all datasets and without varying them during the CLEAN-ing), and only a fraction of the total flux density has been recovered

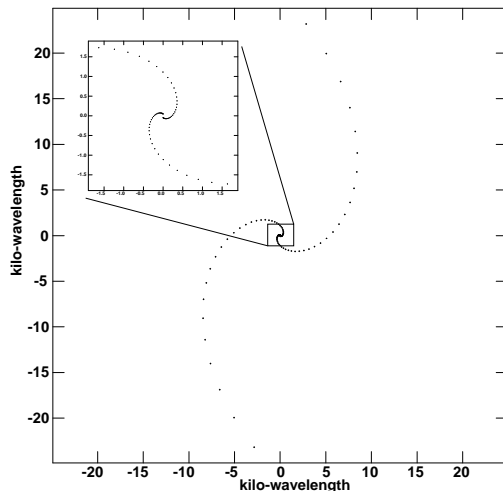


Figure 1: An example of a simulated 2-minute long snapshot uv -coverage outlining relative locations of antenna stations. The largest baseline length, $B_{\max} = 5$ km, and the number of antennas is $N = 50$; In the simulations, only baselines to the central station are considered, resulting in $\Delta u/u \equiv 0.19$ for a full track observation.

after 200,000 iterations, which points out to likely limitations due to application of gridding and deconvolution.

The resulting facet images were stitched together using AIPS task FLATN to create a single final image. We used uniform weighting and the 3D option for the w -term correction throughout our analysis (Cornwell & Perley 1992). In order to assess the effect of deconvolution and gridding of uv -data on the results of the simulations, both the CLEAN and the dirty images were used for estimating several basic FoMs. We use AIPS task IMSTAT to determine the r.m.s. noise levels in each case. The results of these estimates are compared in Fig. 4.

One can see that the dependence of the rms noise (and reciprocally, the dynamic range) on the uv -coverage changes at $\Delta u/u \approx 0.03$. At smaller values of $\Delta u/u$, the uv -coverage does not have a strong effect on the flux density recovered from the visibility data (this holds true for both dirty and CLEAN images). The requirement of

$$\Delta u/u \lesssim 0.03$$

for the entire range of baselines can therefore be used as a benchmark requirement for designing the SKA configurations that would minimise the effect of uv -coverage on reconstructing the sky brightness distribution. It should be noted that this conclusion provides a strong benchmark, implying implementing uv -coverages with uv -gaps larger than 0.03 will limit the imaging capabilities of an array *even with although the present day convolution and imaging algorithms*.

Further, more detailed investigations may be required in order to refine this conclusion and assess the full range of effects that may potentially affect the dynamic range and structural sensitivity derived from images obtained with different uv -coverages and different values of $\Delta u/u$. One possibility would be to use more elaborate and more realistic sky models coming from source simulations (*e.g.*, O’Sullivan et al. 2009).

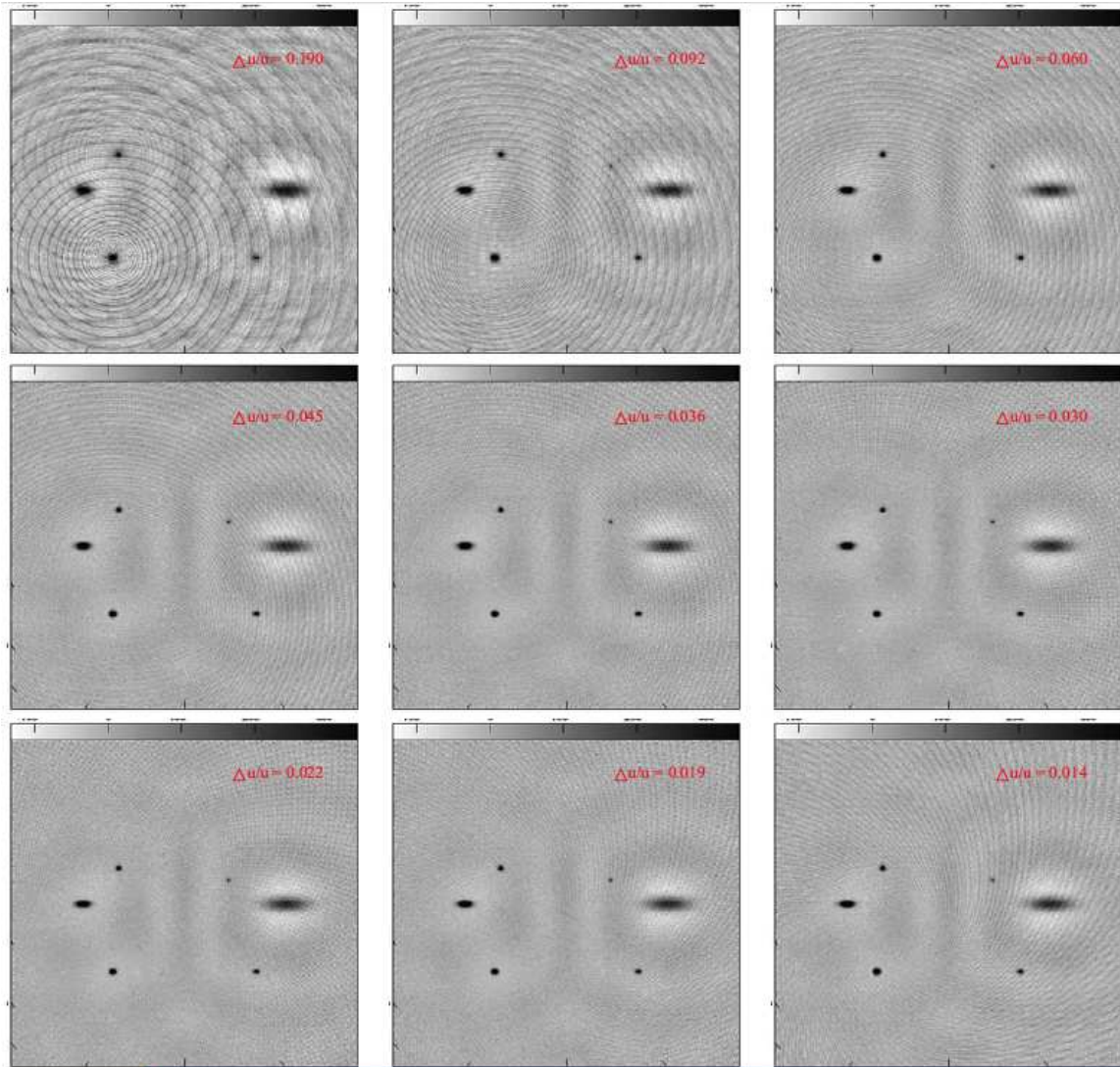


Figure 2: Dirty images obtained from the simulated data. Each panel is marked with the value of $\Delta u/u$ for the respective simulated dataset.

4. Practical issues

We illustrate now a practical way to use the $\Delta u/u$ parameter for evaluating an arbitrary array configuration. The evaluation is based on analysis of a uv -coverage arising from a specific observation or a set of observations (for instance, a number of snapshots on targets covering a specified range of declinations and/or hour angles).

Since almost all real uv -coverages deviate from circular symmetry, the $\Delta u/u$ FoM should be represented either by a two-dimensional distribution or by an average of that. The averaging can be made azimuthally (providing a profile of $\Delta u/u$ as a function of uv -distance) or both azimuthally and radially (giving a single value description of a given uv -coverage). For the averaged quantities, the respective dispersions can be used to quantify inhomogeneities in the uv -coverages.

For the purpose of a better graphical representation of the uv -gap distribution, a definition

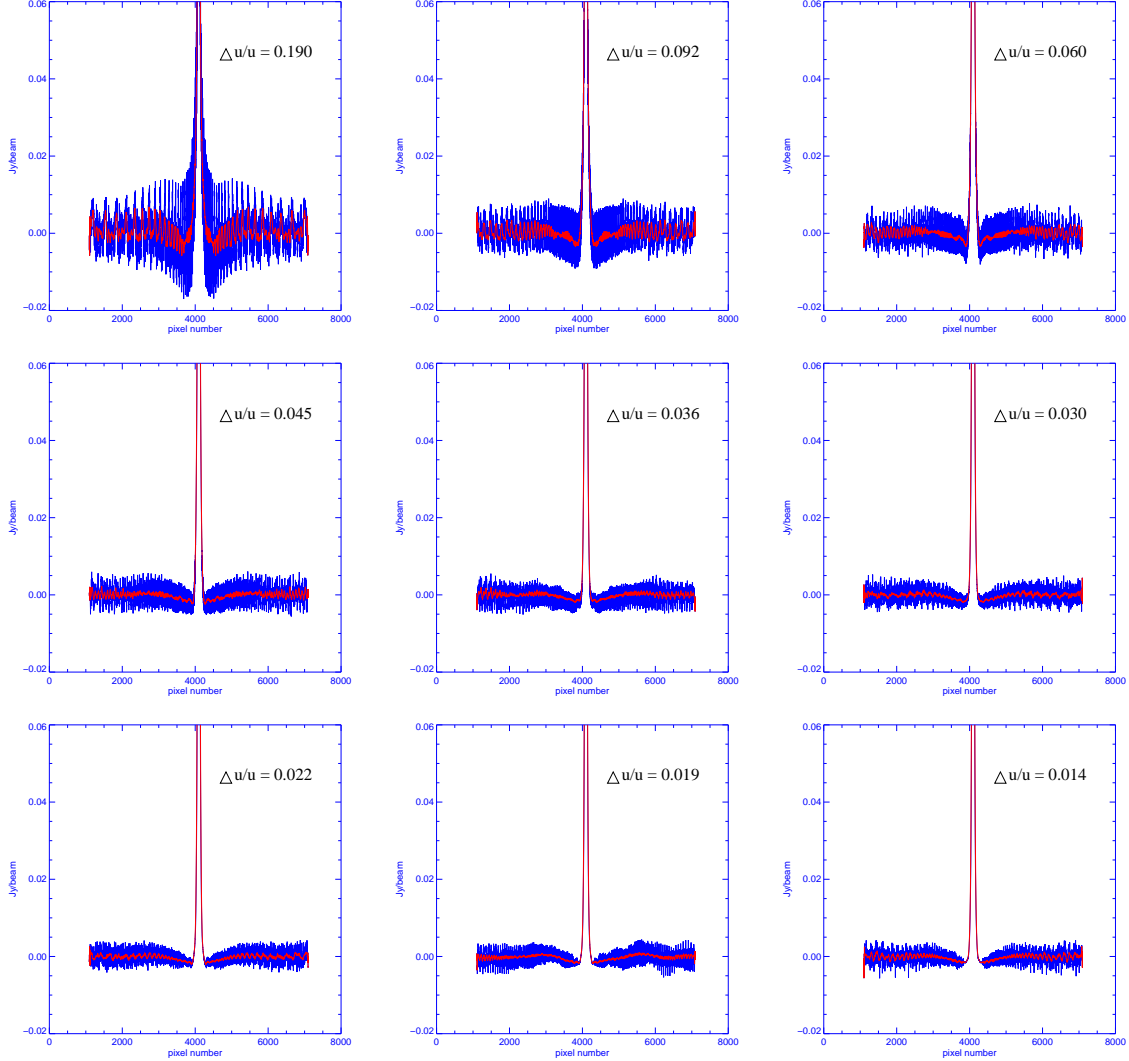


Figure 3: One-dimensional profiles of restoring beams obtained from selected datasets. Each panel shows the value of $\Delta u/u$ corresponding to the respective simulated dataset. The profiles are truncated at 0.06 of the beam peak in order to emphasise the difference in the sidelobes resulting from different uv -coverages. In each panel, the red curve represents the 30-pixel boxcar smoothing of the respective beam profile.

$\Delta u/u = (u_2 - u_1)/u_2$ ($u_2 \geq u_1$) can be applied. This definition changes the range of $\Delta u/u$ from $[0, \infty]$ to $[0, 1]$, with 0 corresponding to $\Delta u/u$ from two identical baselines. The maximum value $\Delta u/u = 1$ is realized everywhere outside the area covered by the observation (for which $u_2 = \infty$ can be assumed).

A feasible approach to determine the figures of merit based on $\Delta u/u$ is as follows:

1. Grid the uv -data into N sectors, where the width of each sector is determined by the observing scan-length (the duration of a snapshot observation, or a typical length of a single scan in a synthesis observation).
2. For each individual sector (described by its central position angle, ϕ_i and width $2\pi/N$ and

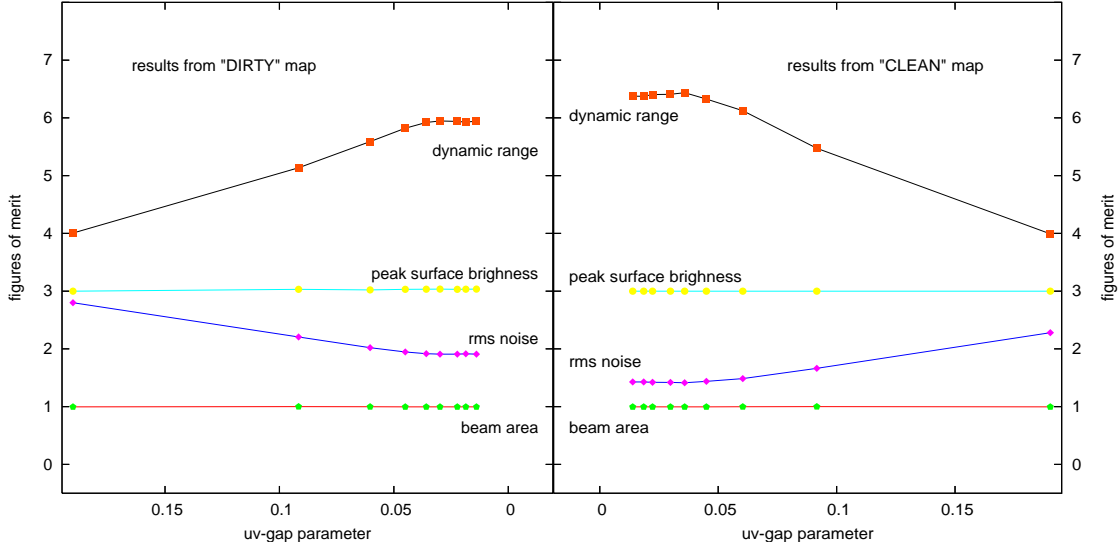


Figure 4: Relative changes of different FoMs obtained from the dirty (left panel) and CLEAN (right panel) maps. The normalization is done with respect to the FoM values determined from the dirty image with $\Delta u/u = 0.01$, by normalizing its beam area to unity, rms noise to the value of 2, peak surface brightness to the value of 3, and dynamic range to the value of 6. The peak surface brightness recovered from different simulation runs remains nearly constant. The rms noise first decreases rapidly for smaller values of $\Delta u/u$, but the rate of this decrease is then remarkably reduced, implying that the uv -coverage does not affect strongly the image noise and dynamic range for array configurations with $\Delta u/u < 0.03$. Note that the dynamic range is determined for a feature with the size substantially smaller than the largest angular scale for the uv -coverage with $\Delta u/u = 0.19$, and thus the calculations are not affected by variable minimum uv -spacing in different simulation runs.

containing M uv -points), determine $\Delta u/u(u, \phi_i)$ for all M uv -points. As was pointed above, $\Delta u/u(u, \phi_i) < 1$ within the range $u_1 \leq u \leq u_M$ and it is equal to unity elsewhere.

3. Plot the combined results for all sectors in polar or rectangular coordinates or perform averaging in azimuth $\langle \frac{\Delta u}{u}(u, \phi) \rangle_\phi$ and/or azimuth and radius $\langle \frac{\Delta u}{u}(u, \phi) \rangle_{u, \phi}$.

A detailed description of the calculation algorithm is given in Appendix 1. Appendix 2 summarizes a proposed set of FoM that includes the uv -gap parameter and can be used for evaluation and optimization of the SKA configuration.

4.1 Examples

In order to represent a two-dimensional distribution $\Delta u/u$, the Voronoi tessellation can be applied to combine the $\Delta u/u$ calculated for the individual sectors. The Voronoi tessellation ("Voronoi diagram") uses partitioning of a plane with n points into convex polygons such that each polygon contains exactly one generating point and every point in a given polygon is closer to its generating point than to any other (Okabe et al. 2000). The Voronoi diagram is sometimes also known as a Dirichlet tessellation. The cells are called Dirichlet regions, Thiessen polytopes, or Voronoi polygons. We use the algorithm by Okabe et al. (2000) built in MATLAB and GNU Octave (version

Table 3: Table showing values of $\Delta u/u$ from azimuthal-radial averaging and the corresponding dispersions for all panels with numbers 1 through 6 in Figs. 6 and 7.

Example uv -coverage	$\langle \Delta u/u \rangle$	$\sigma_{\Delta u/u}$
(1) Simulated log-spiral: core baselines	0.824	0.071
(2) Simulated log-spiral: all baselines	0.219	0.244
(3) Simulated skipped spiral [†] : all baselines	0.203	0.246
(4) VLA snapshot	0.072	0.084
(5) GMRT short observation	0.016	0.043
(6) GMRT nearly full 12 hr synthesis	0.012	0.035

Note: [†] – a multi-arm, logarithmic spiral configuration, with concurrent antennas removed from all but one of the arms of the spiral, in order to reduce the number of redundant baselines as much as possible.

3.2) to decompose the discrete set of $\frac{\Delta u}{u}(uv, \phi_i)$ ($i = 1, N$) values into density plots that can be used as a graphical representation of the uv -gap distribution.

We exemplify this approach by considering six different uv -coverages from simulated and real observations (Fig. 5). The resulting two-dimensional distributions of $\Delta u/u$ are shown in Fig. 6. One can either analyze these distributions directly, or produce azimuthally-averaged radial profiles, or describe these uv -coverages by a single FOM obtained from double, azimuthal-radial averaging. Table 3 shows values of $\Delta u/u$ from azimuthal-radial averaging and the corresponding dispersions for all panels with numbers 1 through 6 shown in Fig. 5.

The radial profiles obtained by azimuthal averaging of the density plots are shown in Fig. 7. One can see immediately, from the profiles in Fig. 7 and the dispersions of the mean in Table 3, that $\Delta u/u$ varies strongly with the baseline length. This dependence should be minimised during the design of the SKA configuration, taking into account the geographical location of the array, the different types of observations (*e.g.*, snapshots, full track synthesis and so on), and the range of declinations for which the imaging performance of the SKA should be optimised.

Acknowledgements

This effort/activity is supported by the European Community Framework Programme 6, Square Kilometre Array Design Studies (SKADS), contract no 011938. SJM has been partially supported by the Spanish DGYCIT grant AYA2006-14986-CO2-02. DVL thanks N. Roy for giving classes on (equiangular) log-spiral, M.A. Voronkov and R.V. Urvashi for helping with the aips++, and is grateful to K. Borkowski and T. Fukushima. for sharing their "Cartesian to geodetic coordinates transform" subroutines. DVL also thanks A.L. Roy for several fruitful discussions and suggestions. We thank the referee, Craig Walker for valuable comments and suggestions.

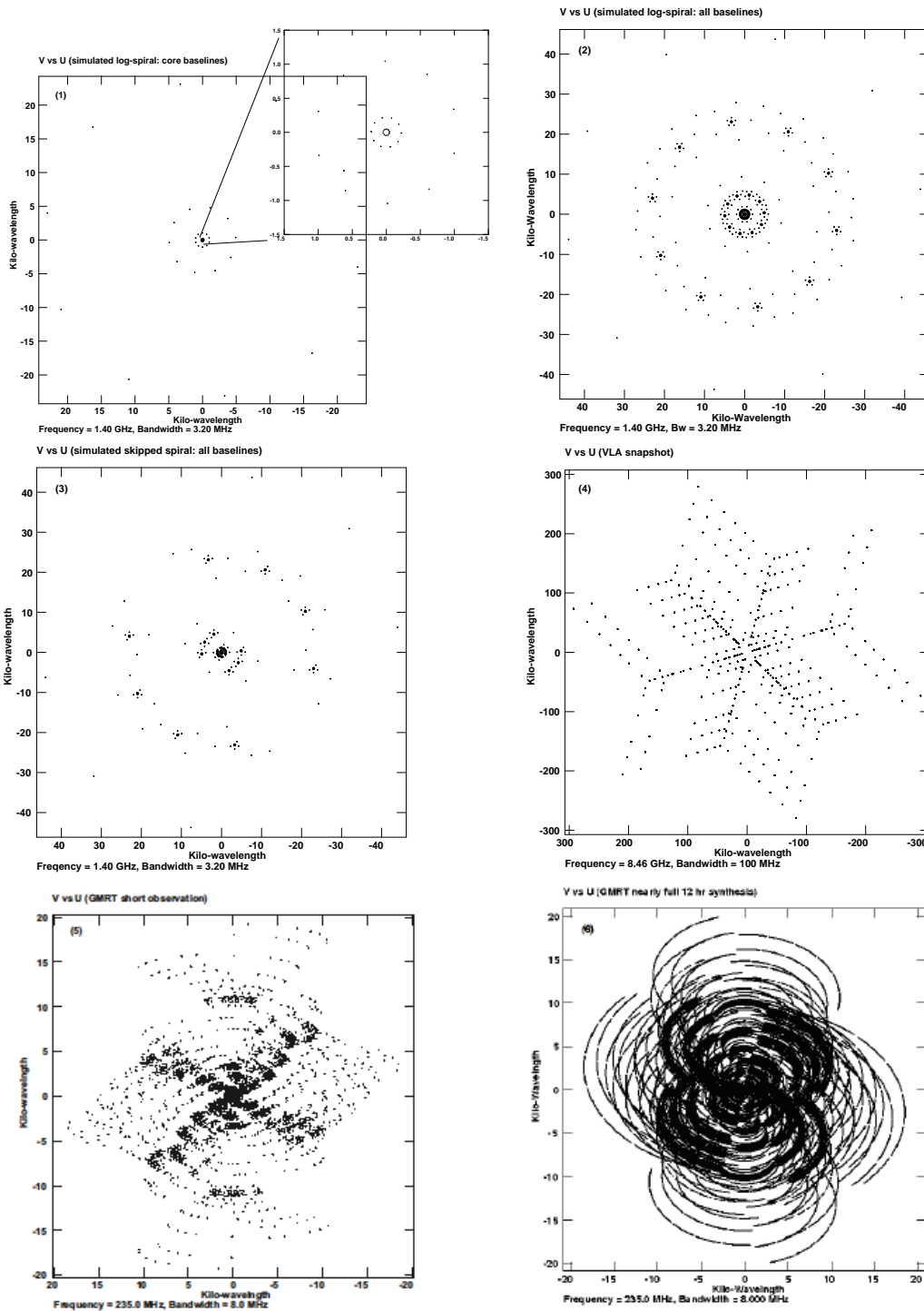


Figure 5: Six different uv -coverages used to exemplify determination of the $\Delta u/u$ figures of merit: (1) a uv -coverage from a simulated log-spiral, baselines to the core station included; (2) the same simulation, all baselines included; (3) a uv -coverage from a simulated skipped-spiral configuration (aimed to provide a nearly constant $\Delta u/u$ and to satisfy the collecting area distribution required for the SKA); (4) a VLA snapshot uv -coverage; (5) a GMRT uv -coverage from a short observation; (6) a GMRT uv -coverage from a nearly complete, 12-hour synthesis.

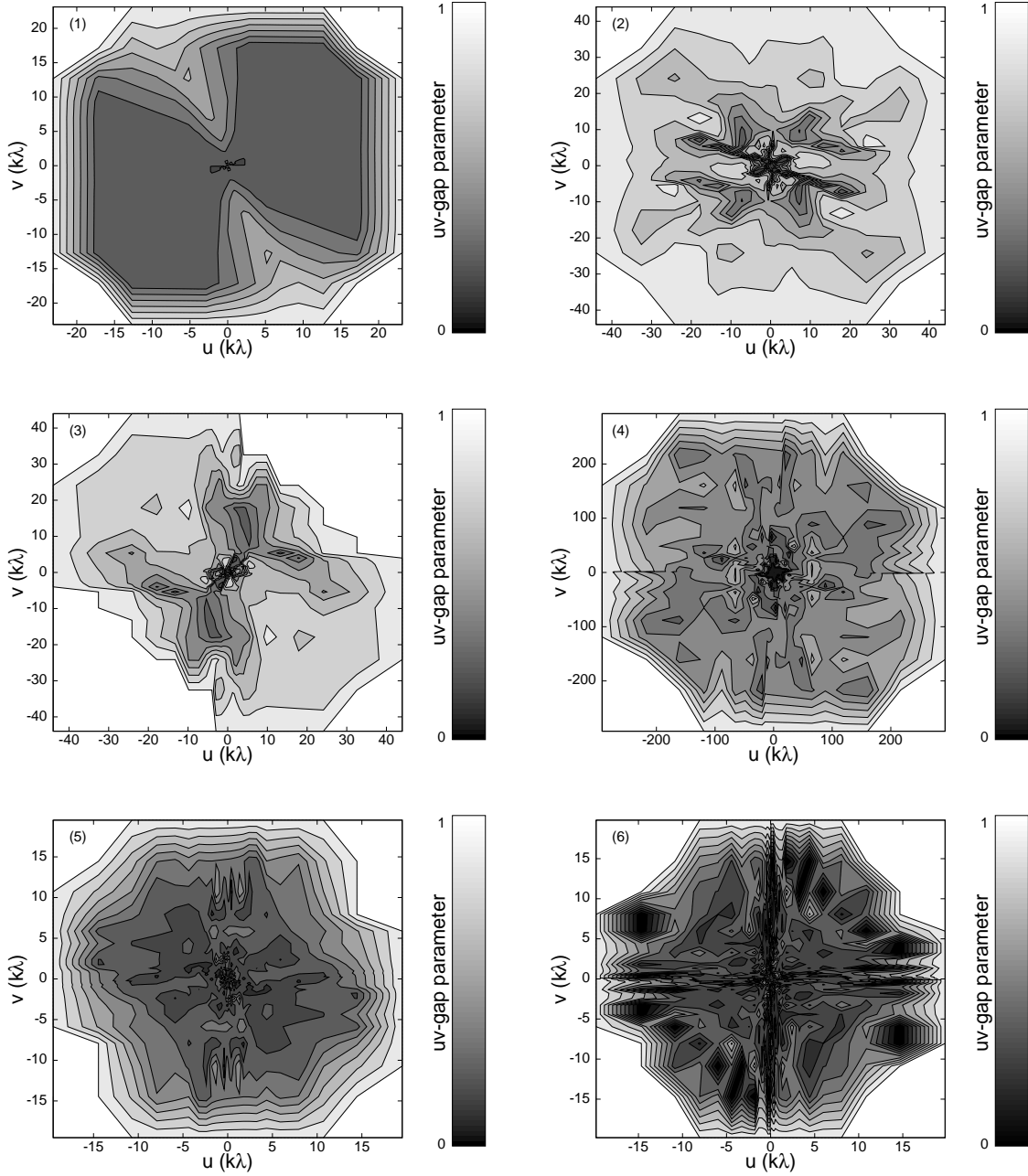


Figure 6: Density plots of $\frac{\Delta u}{u}(u, \phi)$ distribution calculated from the uv -coverages shown in Fig 5. Note that for very sparse uv -coverages, the tessellation algorithm may introduce artefacts. This can be illustrated by the apparent asymmetry of $\Delta u/u$ distribution seen in panel 1 produced for a symmetric uv -coverage with very few uv -points at large uv -radii). More refined approaches to calculating the density fields from uv -coverages may be needed for such cases.

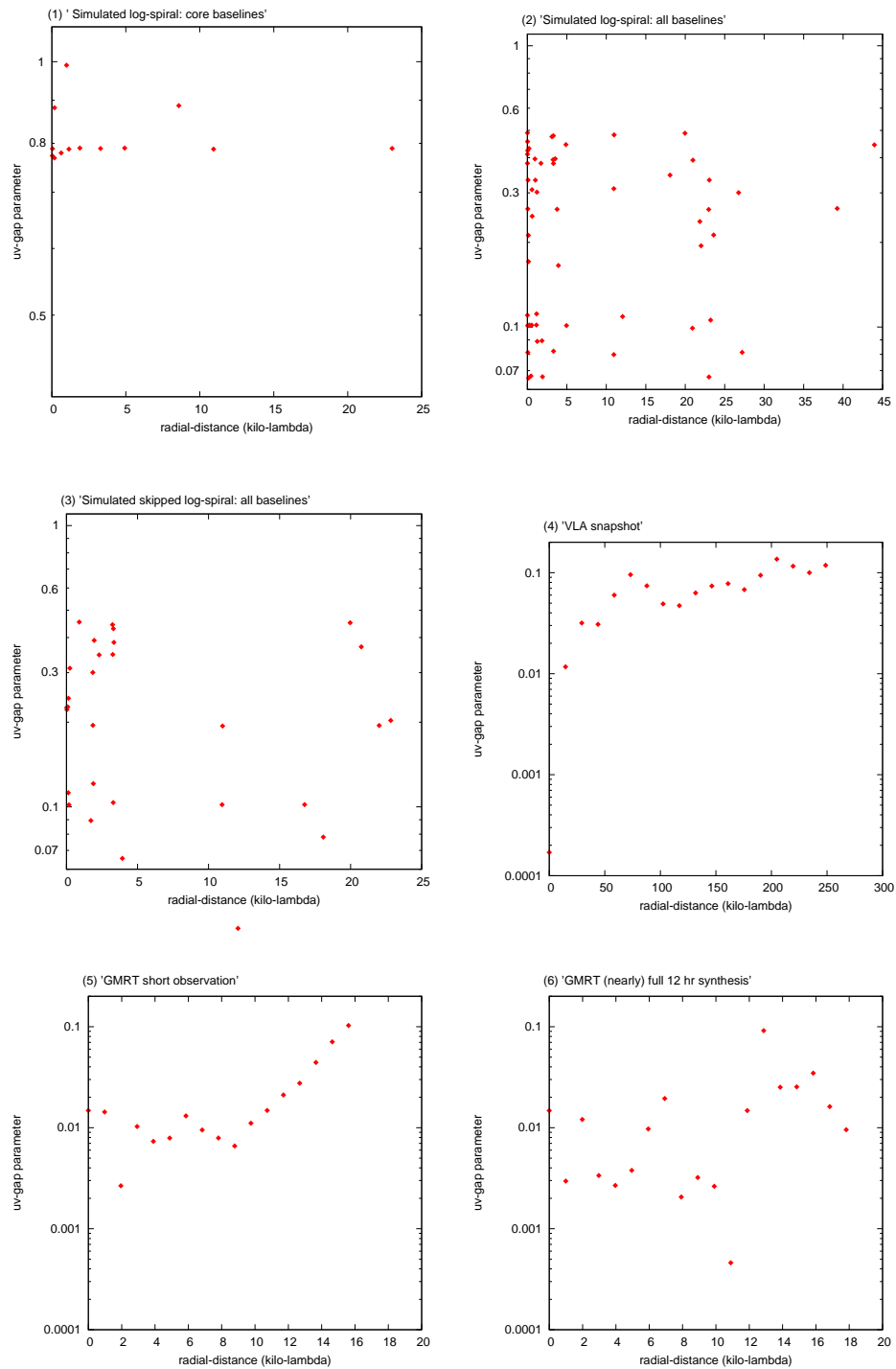


Figure 7: Azimuthally averaged profiles of $\Delta u/u$ from the density plots of $\frac{\Delta u}{u}(u, \phi)$ shown in Fig. 7 for all six cases.

References

- [1] Borkowski, T.J. (1989) "Accurate algorithm to transform geocentric to geodetic coordinates", *Bull. Géod.*, vol. 63, p. 50
- [2] Bregman, J.D. (2000) "Concept design for low frequency array", *SPIE proceedings: Astronomical telescopes and instrumentation, radio telescopes*, vol. 4015, p. 1
- [3] Bregman, J.D. (2005) "Cost effective frequency ranges for multi-beam dishes, cylinders, aperture arrays, and hybrids", *Experimental astronomy* vol. 17, pp. 407–416
- [4] Bridle, A.H. & Schwab, F.R. (1999) "Bandwidth and time-average smearing", *ASP Conf. Series*, vol. 180, p. 371
- [5] Burke, B. & Graham-Smith, F. (2002) "An introduction to radio astronomy", Cambridge (2nd edition)
- [6] Clark, B. (1980) "An efficient implementation of the algorithm CLEAN", *A&A*, vol. 89, p. 377
- [7] Cohanin, B.E., Hewitt, J.N. & de Weck, O. (2004) "The design of radio telescope array configuration using multiobjective optimization: Imaging performance versus cable length", *ApJSS* vol. 15, pp. 705–719
- [8] Conway, J. (1998) "Self-spiral geometries for the LSA/MMA", ALMA memo 216
- [9] Conway, J. (2000a) "Observing efficiency of strawperson zoom array", ALMA memo 283
- [10] Conway, J. (2000b) "A possible layout for a spiral zoom array incorporating terrain constraints", ALMA memo 292
- [11] Cornwell, T.J. (1986) "Crystalline antenna arrays", MM array memo 38
- [12] Cornwell, T.J. & Perley, R.A. (1992) "Radio-Interferometric Imaging of Very Large Fields", *A&A*, vol. 261, p. 353
- [13] Fukushima, T. (2006) "Transforming from Cartesian to Geodetic Coordinated Accelerated by Halley's Method", *Journal of Geodesy*, vol. 79, pp. 689–693
- [14] Heiskanen W.A. & Moritz, H. (1967) "Physical geodesy", WH Freeman, New York
- [15] International SKA Project Office (2006) "Reference design for the SKA", SKA memo 69
- [16] Jones, D.L. (2003) "SKA science requirements", SKA memo 45.
- [17] Kogan, L. (2000a) "The imaging characteristics of an array with minimum side lobes", *ASP Conf. Series*, vol. 217, p. 348
- [18] Kogan, L. (2000b) "Optimizing a large array configuration to minimize the side lobes", *IEEE transactions on antennas and propagation*, vol. 48, p. 1075
- [19] Kogan, L. & Cohen, A. (2005) "Optimization of the LWA antenna station configuration minimising side lobes", LWA memo 21
- [20] Lobanov, A.P., Gurvits, L.I., Frey, S., Schilizzi, R.T., Kawaguchi, N. & Pauliny-Toth, I.I.K. (2001) "VLBI Space Observatory Programme Observation of the Quasar PKS 2215+020: A New Laboratory for Core-Jet Physics at $z=3.572$ ", *ApJL*, vol. 547, pp. 714–721
- [21] Lobanov, A.P. (2003) "Imaging with the SKA: Comparison to other future major instruments", SKA memo 38
- [22] Lonsdale, C.J., Doelman S.S. & Oberoi, D. (2004) "Efficient imaging strategies for next-generation radio arrays", *Experimental Astronomy*, vol. 17, pp. 345–362

- [23] Lonsdale, C.J. (2005) "Configuration considerations for low frequency arrays", ASP Conf. Series, vol. 345, p. 399
- [24] Morita, K.-I. & Holdaway, M. (2005) "Array configuration design of the atacama compact array", ALMA memo 538
- [25] Noordam, J.E. (2001) "Guidelines for the LOFAR array configuration", Project LOFAR, ASTRON, The Netherlands
(<http://www.astron.nl/~noordam/lofar/config.ps>)
- [26] Okabe, A., Boots, B., Sugihara, K. & Chiu, S.N. (2000) "Spatial tessellations – Concepts and applications of Voronoi diagrams", John Wiley (2nd edition)
- [27] O’Sullivan, S.P., Stil, J.M., Taylor, A.R., Ricci, R., Grant, J.K. & Shorten, K. 2009, SKADS Memo 31, www.skads-eu.org
- [28] Perley, R.A. (1999) "High dynamic range imaging", ASP Conf. Series, vol. 120, p. 275
- [29] Perley, R.A. & Clark, B. (2003) "Scaling relations for interferometric post-processing", EVLA memo 63
- [30] Thompson, A.R., Moran, J.M. & Swenson, G.W., Jr. (1986) "Interferometry and synthesis in radio astronomy", New York, Wiley.
- [31] Thompson, A.R., Moran, J.M. & Swenson, G.W., Jr. (2001) "Interferometry and synthesis in radio astronomy", New York, Wiley (2nd edition)
- [32] Voronkov, M.A. & Wieringa, M.H. (2004) "Dynamic range of the SKA images", SimWG report, Sydney
(http://www.narrabri.atnf.csiro.au/~vor010/ska/SimWG_Report2.pdf)
- [33] Voronkov, M.A. & Wieringa, M.H. (2005) "Dynamic range loss due to the retarded baseline effect", SKA memo 68.
- [34] Wright, M.C.H. (2002) "A model for the SKA", SKA memo 16
- [35] Wright, M. (2004) "SKA Imaging", SKA memo 46

Appendix 1: An algorithm for calculating $\Delta u/u$ from uv -coverages

Initial settings

Let us suppose we have a file containing visibilities or a uv -coverage corresponding to an observation with a target array configuration. The uv -coverage is given in polar uv -coordinates (u, θ) and spans a range (u_{\min}, u_{\max}) of uv -distances. Note that the uv -coverage can be completely arbitrary: *i.e.*, it can have asymmetries and gaps along certain position angles — this does not affect the calculation.

The calculation must be done for N individual intervals in position angle. The number N is determined by the dynamic range specification for the array so that $N = \text{SNR}^{1/2}$. This corresponds to a width of $\Delta\theta = 180/\text{SNR}^{1/2}$ degrees for an individual interval and, respectively for a time integration of $\Delta\tau = 720/\text{SNR}^{1/2}$ minutes. For a target $\text{SNR} \rightarrow 10^6$ specified for the SKA, one can assume (for convenience of calculation)

$$\boxed{N = 720, \quad \Delta\tau = 1 \text{ min}, \quad \Delta\theta = 0.25 \text{ deg.}}$$

The uv -tracks on individual baselines should either be generated with an integration time $\Delta\tau$ or averaged to this time (see Step 2 of the calculation).

For convenience of notation, let us denote

$$\boxed{\delta u \equiv \Delta u/u}$$

in the following description of the calculation algorithm.

Calculation of $\Delta u/u$

Step 1. Break the Fourier plane (u, θ) into N intervals in θ (θ -intervals) and N intervals in u (u -intervals), thus forming an $N \times N$ grid in (u, θ) with individual grid cells (u'_i, θ'_j) , with $i = 1, N$ and $j = 1, N$. Note that $\theta \in (0^\circ, 180^\circ)$ and $u \in (0, u_{\max})$.

Step 2. If needed, average the uv -data to $\Delta\tau$ minutes to ensure having one uv -point per baseline per θ -interval.

Step 3. In a given θ -interval, θ_j ($j = 1, N$), add the zero-spacing point ($u_0 = 0$) to the uv -points falling into this interval and calculate (ungridded) values of δu from

$$\delta u_k = (u_k - u_{k-1})/u_k,$$

where $k = 1, M$ and M is the total number of uv -points falling within this θ -interval.

Step 4. For the given θ -interval, θ_j , map the values δu_k to individual grid cells (u'_i, θ'_j) as follows:

$$\forall u'_i \in (u_{k-1}, u_k) : \quad \delta u_i = \delta u_k, \quad k = 1, M, \quad i = 1, N.$$

- For each grid cell, check the following two conditions:

→ If an i -th grid cell contains one of the ungridded values, δu_k , then set its uv -gap value to δu_k — that is, no interpolation between the δu_k and δu_{k+1} is needed for this grid cell.

→ If an i -th grid cell contains several ungridded values of δu , set its δu value by averaging these δu values.

- After mapping the last (M -th) ungridded value of δu , check the following condition:
 - If $u_M < u_{\max}$, assign $\delta u = 1$ to the grid cells falling within the interval (u_M, u_{\max}) , starting from the next grid cell after the cell containing the uv -point u_M .

As a result of this Step, the given θ -interval is divided into N grid cells in u each assigned a value of δu .

Step 5. Repeat Steps 3 and 4 for all θ -intervals and populate the entire (u', θ') grid with uv -gap values $\delta u_{i,j}$, where $i = 1, N$ is the index in u -intervals and $j = 1, N$ is the index in θ -intervals.

Step 6. Plot the gridded distribution $\delta u_{i,j}$ for visual inspection, in the rectangular coordinate system (u, θ) . No smoothing in u or θ is required.

Step 7. Calculate N azimuthal averages of δu

$$\langle \delta u \rangle_i = \frac{1}{N} \sum_{j=1}^N \delta u_{i,j}$$

and their variances

$$\sigma_i^2 = \frac{1}{N} \sum_{j=1}^N (\delta u_{i,j} - \langle \delta u \rangle_i)^2.$$

Step 8. Plot the resulting one-dimensional distribution $(u'_i, \langle \delta u \rangle_i)$, with the respective dispersions, σ_i as errorbars. This gives a radial profile of the uv -gap.

Step 9. Calculate the integral FoM value of δu and its variance from

$$\langle \Delta u / u \rangle_{u,\theta} = \frac{1}{N} \sum_{i=1}^N \langle \delta u \rangle_i,$$

$$\sigma_{\Delta u / u}^2 = \frac{1}{N} \sum_{i=1}^N \sigma_i^2.$$

Various refinements to the procedure described in above can be made. One possibility, for instance, is to calculate $\Delta u / u$ within an angular sector with the width of $\Delta \theta$, then shift this sector by an angle corresponding to the observation intergration time and repeat this procedure until the entire range of the position angles is covered. The resulting distribution of $\Delta u / u$ can be then averaged or smoothed over $\Delta \theta$.

Appendix 2: A set of figures of merit for SKA configuration evaluation

This appendix describes a proposal for an initial set of figures of merit (FoM) for evaluating imaging performance of different array configurations for the SKA. The set of FoM proposed includes general performance metrics and does not include specific requirements on array configuration coming from individual SKA Key Science Projects. The critical issues for evaluating imaging performance provided by a given array configuration are:

1. Providing optimal shape of the point-spread-function (PSF).
2. Minimizing sidelobes of the PSF.
3. Evaluating sensitivity to all spatial scales sampled by the SKA.

Table A1 summarizes a basic set of seven FoM suitable for evaluating the three conditions listed above. The FoM listed in Table 1 are described in polar coordinates in the uv -plane (u, θ) and image plane (r, θ).

Table A1: A set of figures of merit for SKA configuration evaluation

FoM	Description	Name	Goal
Point Spread Function (PSF)	Major Axis	BMA, b_{maj}	$b_{\text{min}}/b_{\text{maj}} \rightarrow 1$
	Minor Axis	BMI, b_{min}	
	P.A. of Major Axis	PAN, θ_{maj}	$B(r, \theta) \rightarrow \text{Gaussian}$
	PSF Shape	PSF, $B(r, \theta)$	
PSF Sidelobes	Maximum Positive Sidelobe	MPS, σ_+	$\sigma_+ \rightarrow 0$
	Maximum Negative Sidelobe	MNS, σ_-	$\sigma_- \rightarrow 0$
	Sidelobe RMS	RMS, σ_{rms}	$\sigma_{\text{rms}} \rightarrow 0$
UV Gap	Integrated Value	UVG, $\Delta u/u$	$\langle \Delta u/u \rangle_{u, \theta} \rightarrow 0$
	Dispersion	UVD, $\Delta u/u(u, \theta)$	$\sigma_{\Delta u/u} \rightarrow 0$